Geophysical Research Letters, Accepted on 12 December, 2022

Slow Fault Slip Signatures in Coseismic Ionospheric Disturbances

K. Heki[1,2], M. S. Bagiya[3], and Y. Takasaka[2]

[1]Shanghai Astronomical Observatory, Chinese Academy of Sciences, Shanghai, China

[2]Dept. Earth Planet. Sci., Hokkaido University, Sapporo, Japan

[3]Indian Institute of Geomagnetism, Mumbai, India

Corresponding author: Kosuke Heki (heki@sci.hokudai.ac.jp)

.

Key Points:

- Large earthquakes excite atmospheric waves with various periods that propagate upward and disturb the ionosphere
- Empirical relationship between earthquake magnitudes and amplitudes of internal gravity waves is established using satellite signals
- Tsunami earthquakes, characterized by slow fault sips, are found to excite longer period atmospheric waves more efficiently.

Abstract

Rise times of earthquake moment release influence the spectra of seismic waves. For example, slow fault movements in tsunami earthquakes excite larger tsunamis than expected from intensities of short-period seismic waves. Here we compare amplitudes of two different atmospheric waves, long-period internal gravity waves and short-period acoustic waves, excited by coseismic vertical crustal movements. We observe them as coseismic ionospheric disturbances by measuring ionospheric electrons using global navigation satellite systems. Four regular megathrust earthquakes M_w 8.0-9.0 showed that the internal gravity waves become ten times stronger as the magnitude increases by one. We found that the 2010 Mentawai earthquake, a typical tsunami earthquake, excited internal gravity waves stronger than those expected by this empirical relationship. On the other hand, amplitudes of acoustic waves excited by tsunami earthquakes were normal. This suggests that slow fault ruptures excite long-period atmospheric waves efficiently, leaving a slow earthquake signature in ionospheric disturbances.

Plain Language Summary

Rapidly moving objects excite short-period waves, and slow objects excite long-period waves. We confirmed this for atmospheric waves excited by vertical crustal movements associated with large earthquakes. Two kinds of atmospheric waves, long-period internal gravity waves and short-period acoustic waves, propagate upward hundreds of kilometers and disturb the Earth's ionosphere. They are observed by receiving dual-frequency microwave signals from satellites. We compared atmospheric wave amplitudes excited by ordinary earthquakes and by "tsunami" earthquakes, characterized by slow fault movements. We found that the 2010 Mentawai earthquake, a typical tsunami earthquake, excited abnormally large internal gravity waves from ionospheric observations. This is the first slow earthquake signature found in space.

1 Introduction

Frequency spectra of seismic waves from a ruptured fault reflects fault sizes, i.e., those by larger magnitude earthquakes are richer in longer-period seismic waves. They also reflect rupture speeds of faults. Tsunami earthquakes are defined as those exciting large tsunamis for their surface wave magnitudes (Kanamori, 1972). They show large departure between surface wave magnitudes (M_s) and moment magnitudes (M_w), as represented by the 1896 Meiji-Sanriku earthquake, NE Japan, with M_s=7.2 and M_w=8.0 (Tanioka and Satake, 1996). Such departure would be due partly to the small rigidity of soft sediments near trenches. It is also due to slow faulting, i.e., a longer duration of fault slip may excite tsunamis more efficiently than ordinary earthquakes. Does this apply for atmospheric waves caused by coseismic vertical crustal movements?

We could answer this question by observing ionospheric disturbances using dual-frequency global navigation satellite system (GNSS) receivers. Atmospheric waves from epicenter propagate upward and often disturb ionospheric F region, typically ~300 km high. They are observed as changes in ionospheric total electron content (TEC), number of electrons along the line-of-sights connecting GNSS receivers and satellites. Since its first observation by Calais and Minster (1995) with Global Positioning System (GPS), the oldest GNSS, lots of coseismic

ionospheric disturbances have been reported using the GNSS-TEC technique (e.g., Tanimoto et al., 2015; Jin et al., 2015; Jin et al., 2018; Meng et al., 2019; Astafyeva, 2019; Heki, 2021).

Initial disturbances caused by acoustic waves typically have periods of ~4 minutes and emerge ~10 minutes after earthquakes. They propagate in two different velocities, ~0.8 km/s (acoustic waves from epicenters) and ~4 km/s (acoustic waves excited by propagating Rayleigh waves). Here we call the former AW, and the latter RW. For very large earthquakes, they are followed by internal gravity waves (IGW), with periods of 10-20 minutes, propagating by 0.2-0.3 km/s.

Amplitudes of the ionospheric disturbances caused by near-field AW, relative to background vertical TEC (VTEC), correlate well with earthquake magnitudes. For example, Heki (2021) showed that the relative AW amplitudes get ~100 times as large for the increase of M_w by three. We begin our study by establishing such relationship for IGW. We then focus on ionospheric disturbances of recent tsunami earthquakes and discuss their uniqueness in exciting AW and IGW.

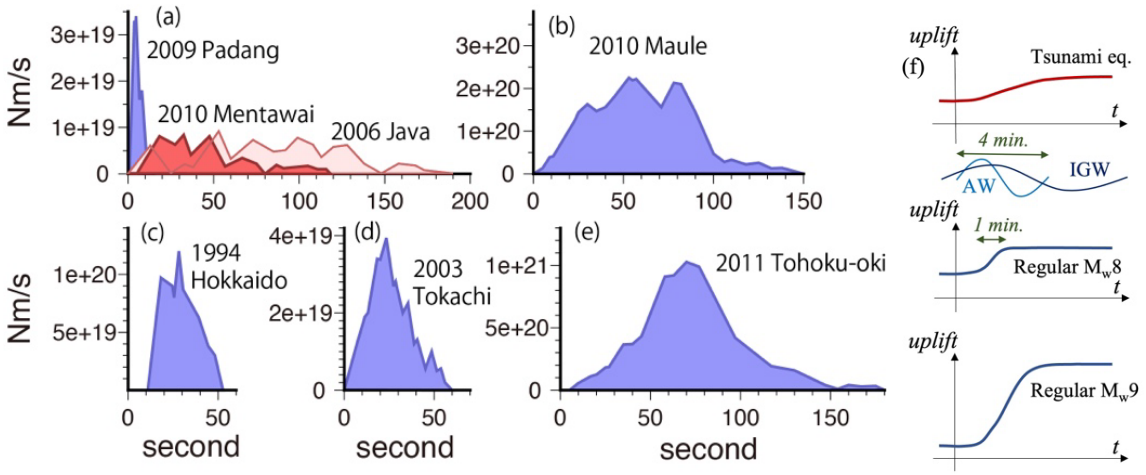

Figure 1 (a) Source time functions of two similar magnitude earthquakes in Sumatra (2009 Padang and 2010 Mentawai) after Satake et al. (2013). The function for the 2006 Java earthquake (Ammon et al., 2006) is also added. The 2010 Mentawai and 2006 Java earthquakes are known as typical tsunami earthquakes. (b)-(e) show those for four large earthquakes, (b) the 2010 Maule (M_w8.8) (Pulido et al., 2011), (c) 1993 Hokkaido-toho-oki (M_w8.3) (Kikuchi and Kanamori, 1995), (d) 2003 Tokachi-oki (M_w8.0) (Yagi, 2004), and (e) the 2011 Tohoku-oki (M_w9.0) (Yagi and Fukahata, 2011) earthquakes. Larger earthquakes have longer durations of faulting. The two tsunami earthquakes in (a) show anomalously long duration for their magnitudes. (f) compares images of crustal uplift of regular M_w8 and 9 earthquakes and a tsunami earthquake, together with the two atmospheric waves.

Figure 1 shows the source time functions of earthquakes studied here. Faulting takes less than a minute for typical M8 class earthquakes (Figure 1c, d), while it continues for a few minutes for M9 class events (Figure 1b, e). Figure 1a compares the source time functions of a tsunami earthquake, the 2010 October Mentawai earthquake, Indonesia, with a similar magnitude "regular" earthquake (i.e., not a tsunami earthquake) in Indonesia. The Mentawai earthquake is a typical tsunami earthquake with a long-lasting low-level moment release (Lay et al., 2011), and Satake et al. (2013), by tsunami waveform inversion, inferred its M_w as 7.9. Figure 1a includes

another tsunami earthquake, the 2006 July Java earthquake (M_w7.8) (Ammon et al., 2006; Fujii and Satake, 2007).

Meng et al. (2019) suggested that regular earthquakes excite mainly AW by rapid crustal movements, while slow vertical sea surface motions by tsunamis in an open ocean only excite IGW. Indeed, the typical duration of coseismic uplift of a regular M_w8 event is equivalent to a quarter of the AW period (~1 min.) (Figure 1f) suggesting its efficient excitation. On the other hand, IGW periods are much longer, and they would be more efficiently excited by earthquakes where uplifts take minutes or more. In this article, we will compare amplitudes of direct AW and IGW excited by earthquakes in Figure 1a-e, expecting their anomalous amplitudes for tsunami earthquakes.

2 IGW signatures in TEC

2.1 TEC data

Heki (2021) presents AW signatures from 28 earthquakes, but these earthquakes do not necessarily show clear signatures of direct IGW from epicenters. The IGW signals are weaker than AW and become visible only for earthquakes with M_w 8 or more. Faint IGW signatures could be recognized as linear features having prescribed slopes in the time-distance plots. Hence, we need a dense network of ground GNSS receivers to study IGW amplitudes. Here we select M_w 8-9 events with sufficient density and coverage of GNSS stations recording coseismic ionospheric disturbances.

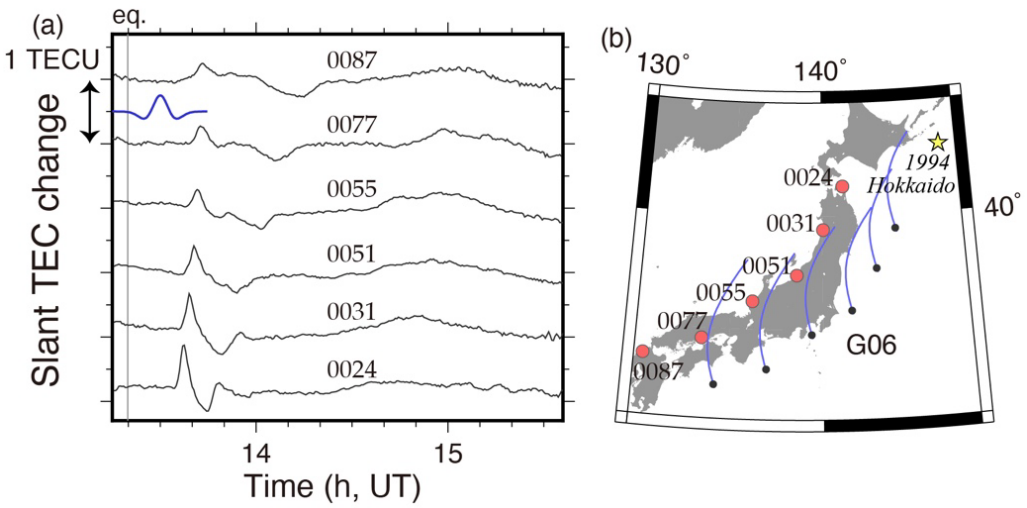

Figure 2 (a) Time series of slant TEC of satellite G06 as the residuals from best-fit quadratic functions at six GNSS stations in Japan. The data include coseismic ionospheric disturbance signatures of the 1994 Hokkaido-toho-oki earthquake. We can recognize signatures of the three different atmospheric waves, AW, RW, and IGW, propagating in different velocities. A blue curve shows a wavelet used to extract 12-minute period component in Figure 3. (b) Map showing the GNSS station positions and the SIP tracks of satellite G06 during the period shown in (a) (blue dots show the earthquake occurrence time). The ionosphere was assumed as a thin layer as high as 300 km here.

For the 1994 Hokkaido-toho-oki, 2003 Tokachi-oki, and 2011 Tohoku-oki earthquakes, we used data from the dense Japanese network of GNSS stations, known as GEONET (GNSS Earth

Observation Network). For the 2010 Maule earthquake, we obtained data from Chile and Argentine, the same data set as in He and Heki (2016). We used the Sumatra GPS Array (SUGAR) data and a few additional stations operated as International GNSS Service (IGS) stations to study the 2010 Mentawai earthquake. For the 2006 Java earthquakes, we could use only IGS stations because SUGAR stations are not close enough to the epicenter. We calculated TEC from raw data files following Heki (2021). Here we call the GPS satellite PRN6 as G06.

2.2 IGW signatures of regular earthquakes

Figure 2a shows an example of coseismic ionospheric disturbances as slant TEC time series over a two-hours period following the 1994 Hokkaido-toho-oki earthquake (M_w8.3), originally studied by Astafyeva et al. (2009). They are characterized by strong initial peaks ~10 minutes after the earthquake, and subsequent smaller and slower components. IGW signatures appear as subtle changes in trend 14:30-15:00 UT. These time series show residuals from best-fit quadratic functions, and these IGW signatures easily disappear by using higher-degree polynomials. After all, we found it difficult to recognize IGW signals by plotting residuals from best-fit polynomials.

Wavelet transformation is an effective way in extracting coseismic disturbance signals from TEC time series (Heki and Ping, 2005). Because we do not subtract best-fit polynomials, we can get results with a more objective manner. In Figure 3, we show results of the wavelet transformation to the raw TEC time series emphasizing components with periods around 12 minutes plotted as a function of time and focal distance. It shows examples of the 1994 Hokkaido-toho-oki and the 2010 Maule earthquakes.

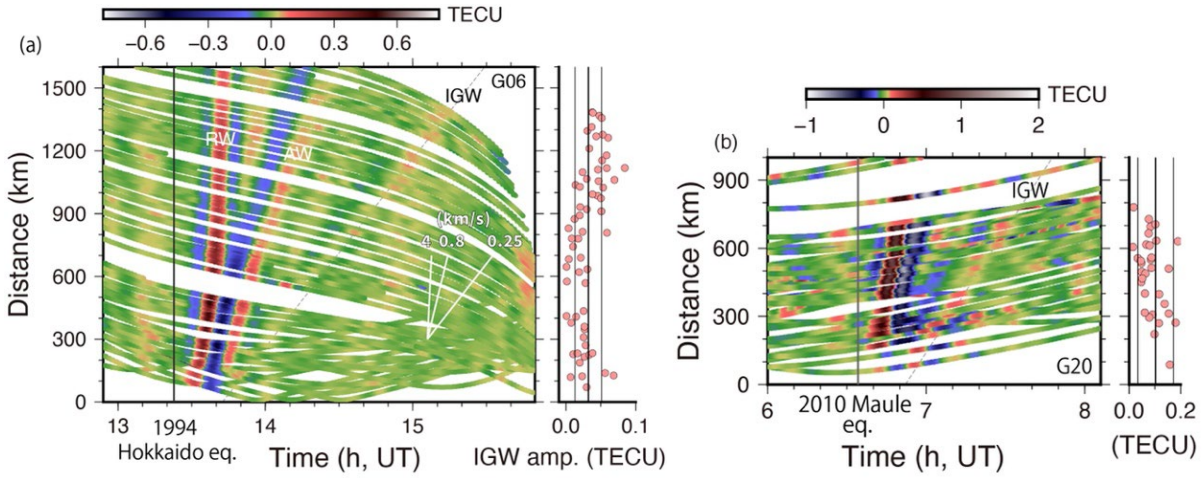

Figure 3 (a) A time-distance plot of coseismic ionospheric disturbances for the 1994 Hokkaido-toho-oki earthquake by the three different atmospheric waves RW, AW, and IGW, with velocities of ~4, ~0.8, and ~0.25 km/s, respectively (slopes given by white lines). (b) Same plot for the 2010 Maule earthquake. RW and AW are not well separated in this distance range, but IGW signatures are clear. To the right, we show IGW amplitudes for various focal distances (lines indicate the means and the standard deviations, a:0.032±0.019, b:0.103±0.069). In both cases, we use the 12 minutes wavelet.

The direct AW signatures look like signals propagating by ~0.8 km/s after reaching the ionosphere in ~10 minutes. In Figure 3a, a faster (~4 km/s) component due to RW well separates from AW over distances exceeding 600-700 km. The RW and AW signatures do not separate

well for the 2010 Maule earthquake (Figure 3b) because the distances are mostly < 700 km. In both cases, we could recognize IGW signatures as linear positive anomalies having a slope of 0.25 km/s occurring after the RW/AW passages. Figure S1 demonstrates that AW components get clearer by using shorter-period wavelets, while IGW becomes more evident as we increase the wavelet period. In this study, we used a 12-minutes wavelet for all the cases to infer IGW amplitudes. An empirical factor, derived by performing a wavelet transformation for a sine curve with a known amplitude, has been multiplied to obtain IGW amplitudes.

In these earthquakes, IGW signatures show propagation velocities, ~0.25 km/s (Figure.3a) and ~0.30 km/s (Figure 3b). Their hypothetical intersections with the zero distance lines are ~20 minutes after the earthquake for both cases (IGW propagates obliquely upward and does not actually emerge right above epicenters). IGW signals typically emerge 30-40 minutes after earthquakes a few hundreds of kilometers away from epicenters (e.g., Matsumura et al., 2011).

For the two cases given in Figure 3, we obtain amplitudes of IGW signatures for individual satellite-station pairs and show them to the right. We do not recognize any spatial decays over these distance ranges. On the contrary, in Figure 3a, we observe somewhat stronger peaks for signals at distances exceeding 1,000 km. This may reflect the change in geometry between the line-of-sights and wavefronts, i.e., the angle between them may have become smaller for later times as satellite G06 moves northward (Figure 2b). We simply calculate the mean amplitudes and use them to discuss their M_w dependence.

In the supplementary materials, we show examples of the 2003 Tokachi-oki (Figure S2) and the 2011 Tohoku-oki (Figure S3) earthquakes as additional examples of M8 and M9 class earthquakes. In Figure S3, there are two signatures with velocities ~0.25 and ~0.21 km/s. We selected the slower one as the true IGW signature, but the conclusion would not change by selecting the faster one. We also analyzed a few more earthquakes, with enough GNSS data, looking for IGW signatures, i.e., the 2007 Bengkulu earthquake (M_w8.5) (Cahyadi and Heki, 2013), the 2006/2007 doublet (M_w8.2/8.1) in the central Kuril Islands (Astafyeva and Heki, 2009), and the 2015 Illapel earthquake (M_w8.3) in Chile (He and Heki, 2016). However, we could not find clear IGW signatures due to insufficient number of stations and/or insufficient background TEC. Regarding the 2004 Sumatra-Andaman earthquake (M_w9.2), data from a dense network in Malaysia are available. However, the east-west dimension of the network (~200 km) does not provide enough range of the focal distance to accurately constrain the propagation velocity of the anomalies.

2.3 Scaling law for regular earthquakes

Here we compare amplitudes of the two different waves, AW and IGW, for the four earthquakes, i.e., the 2011 Tohoku-oki, 2010 Maule, 1994 Hokkaido-Toho-Oki, 2003 Tokachi-oki earthquakes, in Figure 4a. For their AW amplitudes, we use the values from Cahyadi and Heki (2015). We find that the IGW amplitudes have a stronger magnitude dependence than AW, i.e., amplitude becomes ~10 times stronger for a magnitude increase by one. This justifies that it is difficult to identify IGW for earthquakes of M_w<8 because their amplitudes would not exceed 0.2% of background VTEC.

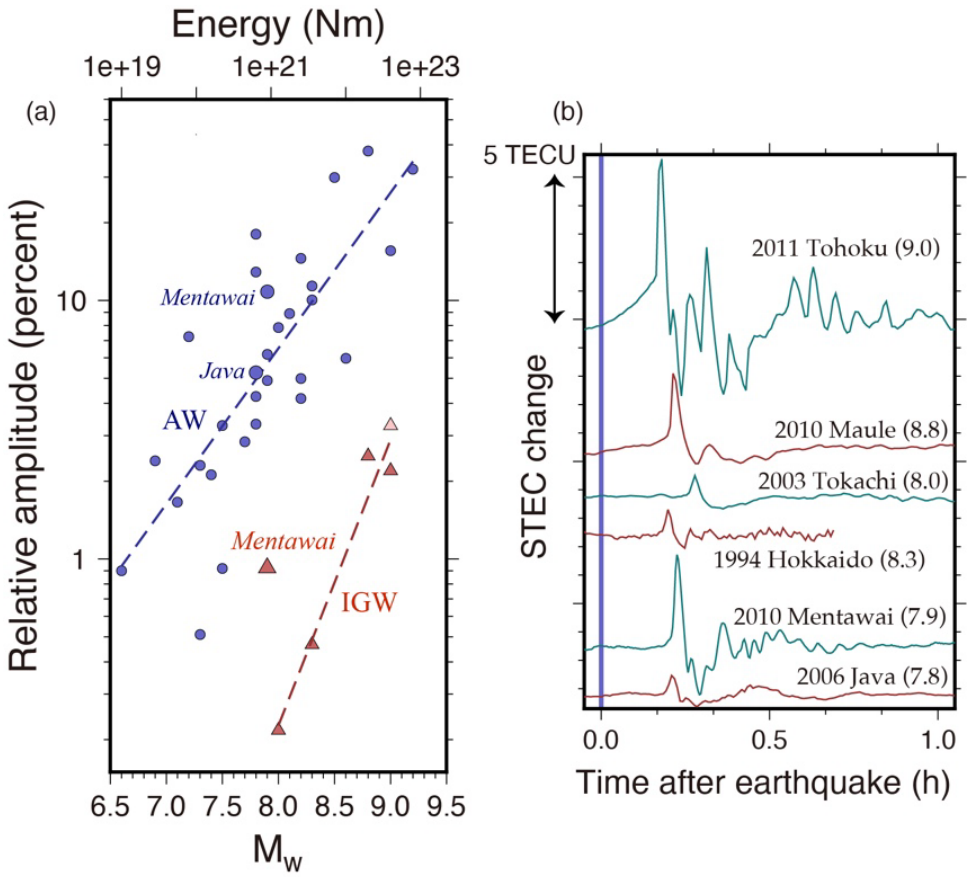

Figure 4 (a) AW (blue circles) and IGW (red triangles) amplitudes as a function of M_w of earthquakes. IGW data for five earthquakes and two AW data for the tsunami earthquakes are added to Figure 21.5 in Heki (2021). Symbols for the tsunami earthquakes are enlarged (no clear IGW signals for the 2006 Java event). A pink triangle corresponds to the wave indicated as "IGW?" in Figure S3. (b) compares coseismic ionospheric disturbance records in slant TEC for the six earthquakes studied here. The data are from Heki (2021) except for the two tsunami earthquakes (their station-satellite pairs are abgs-G29, and bako-G03, for the 2010 and 2006 earthquakes, respectively).

The M_w dependence of the AW amplitudes (blue dashed line in Figure 4a) would reflect the spatial properties of coseismic uplift, e.g., its amount and area (Cahyadi and Heki, 2015), but it is not clear if the duration of faulting also matters. A steeper slope for IGW (red dashed line) suggests the importance of the temporal factor, duration of faulting, i.e., a longer period of coseismic vertical crustal motion may excite IGW more efficiently (Figure 1). Tanimoto et al. (2012) suggested that main ruptures in megathrust earthquakes may be followed immediately by afterslips lasting for minutes, and they are responsible for the excessive excitations of low-frequency constituents of the Earth's free oscillation. Such continuing slips may also contribute to the efficient generation of IGW.

Here, we recall that we investigate IGW propagating directly from epicenters, and do not discuss IGW from tsunami propagating in an open ocean, which are often detected in far-fields, e.g., in Hawaii after the 2011 Tohoku-oki earthquake (Makela et al., 2011; Savastano et al., 2017). As seen in Figure S4, we observe IGW generated at focal areas and propagating above land areas without significant interactions with propagating tsunamis.

2.4 Tsunami earthquakes

Next, we study amplitudes of AW and IGW for two tsunami earthquakes, the 2010 Mentawai (M_w7.9) and the 2006 Java (M_w7.8) earthquakes. Their AW signatures, together with the four regular earthquakes, are given in Figure 4b, and their relative amplitudes are included as large blue dots in Figure 4a. We do not see anomalous amplitudes for AW of these two tsunami earthquakes, although the Mentawai earthquake excited AW with an amplitude somewhat larger than average reflecting its shallow epicenter and consequent large coseismic vertical movements (Manta et al., 2020). For an extremely slow faulting (with durations of hours or longer), no atmospheric waves would be excited. In this sense, their "slow" moment releases (Figure 1a) were fast enough to excite AW with periods of ~4 minutes.

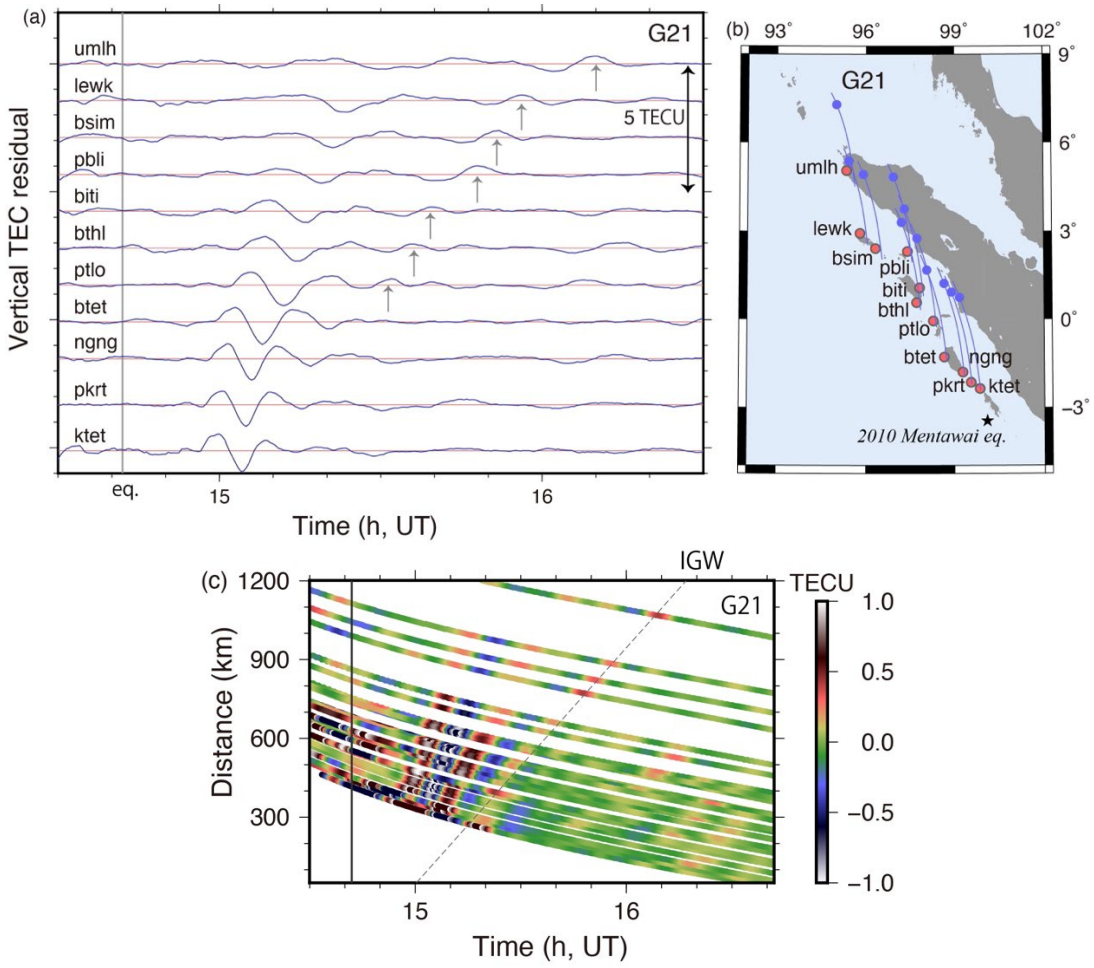

Figure 5 (a) Vertical TEC changes (residual from degree 7 polynomials) at 11 stations for satellite G21 arranged from south (bottom) to north (top) after the 2010 Mentawai earthquake. We could see the IGW signals for many of the stations (gray arrows). The station positions (red dots) and SIP trajectories are given in (b). Blue dots in the trajectory indicate the earthquake occurrence time (SIPs move southward). (c) Distance-time plot of the wavelet-transformed (12 minutes) STEC time series. The dashed line indicates possible IGW signature, with a speed of 0.25 km/s and hypothetical intersection with zero-distance at 15 minutes after the earthquake.

Next, we study their IGW signatures. Figure 5a shows vertical TEC of G21 as viewed from 11 SUGAR stations deployed mainly on islands west of Sumatra. In addition to fast AW components, we recognize the existence of a slow component with amplitudes of 0.2-0.3 TECU. In the time-distance plot (Figure 5c), these anomalies line up along a slope of 0.25 km/s manifesting an IGW signature. The average IGW amplitude of all the stations, derived in the same way as the regular earthquakes with STEC, was ~0.24 TECU, which is ~0.92% of the background VTEC. This is >5 times as large as the value expected for an M_w7.9 earthquake from the trend of regular earthquakes (Figure 4a, red dashed line).

As for the 2006 Java tsunami earthquake, we had only two IGS stations (xmis and bako) within 300 km from the epicenter. SUGAR stations, used for the 2010 Mentawai earthquake, are too far to study the IGW signature. Figure S5 shows a few time series together with the time-distance plot. They might include IGW signals, but it is difficult to confirm its propagation velocity and to constrain their amplitudes. Indeed, despite similar M_w of these two tsunami earthquakes, background VTEC of the 2006 Java event is ~1/3 of the 2010 Mentawai event. So, its IGW amplitudes would be weaker than the 1994 Hokkaido-toho-oki earthquake. It would be difficult to identify such faint IGW signals without dense networks like GEONET. Here, we present only the AW amplitude and do not discuss its IGW amplitude.

3 Discussion and conclusions

3.1 Sources of errors

A few remaining problems include the influence of geomagnetism in IGW amplitudes (Occhipinti et al., 2008). If the motions of neutral particles are orthogonal to the geomagnetic fields, no disturbances in electron contents are observed (Georges and Hookes, 1970). The IGW discussed here falls into the category of medium scale waves. They typically have wavefronts of 45 degrees from the vertical, and neutral particles move perpendicular to the direction of phase propagation (Hargreaves, 1992). This suggests that a certain factor coming from geomagnetic inclination may govern the IGW amplitudes (Figure S6). In the five earthquakes whose IGW signatures were found, the shallowest inclination occurs for the 2010 Mentawai earthquake (-24.7 degrees), and the steepest inclination occurs for the 1994 Hokkaido-toho-oki earthquake (+57.5 degrees). This range of geomagnetic inclination would only moderately influence the growth of electron density disturbances, and we think it unlikely that the relatively shallow inclination in the Mentawai case caused the anomalously large IGW amplitude.

Geometry of the line-of-sight and wavefront controls AW amplitudes in TEC, and a large signal is expected when the line-of-sight penetrates the wavefront with a shallow angle (e.g., Bagiya et al., 2019; Heki and Fujimoto, 2022). Such relationship is not well understood for IGW. We consider that line-of-sights closer to the direction of geomagnetism may record smaller amplitudes because they penetrate both positive and negative anomalies. In most cases studied here, line-of-sights have enough angles from local geomagnetic fields enabling the IGW signature detections. This is not really the case for the 2003 Tokachi-oki earthquake (Figure S2). When the IGW signature emerged (~20:30 UT), line-of-sight was >20 degrees apart from the geomagnetic field, but the angle became less as the satellite moves southward. This may explain that the IGW signature is lost after 21:30 UT. A future revision of the IGW part of Figure 4a considering such geometry factors would improve the empirical relationship between IGW amplitudes and M_w. The details of the geomagnetism and geometry problems are discussed quantitatively in Heki and Fujimoto (2022).

Another concern is the contribution of the IGW excited by the propagating tsunami in the 2010 Mentawai case. SIPs were above the chain of islands off the west coast of Sumatra when the IGW signals are recorded (Figure 5b). Although the amplitudes of tsunamis near the epicenter exceeded 5 meters, those recorded at these islands are a few tens of centimeters or less (Satake et al., 2013). We assume that the tsunami propagating over the studied area would not have significantly contributed to the large amplitude of IGW.

3.2 Conclusions

The first conclusion of the paper is the strong M_w dependence of the IGW amplitudes for regular earthquakes. By comparing IGW amplitudes in coseismic ionospheric disturbances of M_w8-9 megathrust earthquakes, we found that they have a larger magnitude dependence than AW, i.e., a larger earthquake has a larger IGW/AW ratio. This suggests that the time constants of faulting may play a larger role in exciting IGW than AW.

The second conclusion is on the ionospheric disturbances of tsunami earthquakes. We studied the two recent tsunami earthquakes in Indonesia, the 2010 Mentawai and 2006 Java earthquakes. Although we could not identify IGW signatures for the latter due to weak signals and insufficient nearby GNSS stations, we found an abnormally strong IGW signature for the former. This further supports the idea that longer durations of faulting favor efficient excitations of longer period atmospheric waves. We also found that the AW amplitudes of these tsunami earthquakes were not significantly different from regular earthquakes.

Acknowledgements

This research was supported by JSPS KAKENHI Grant number JP20K04120. K.H. is also supported by Chinese Academy of Sciences, President's International Fellowship Initiative (Grant number 2022VEA0014). We thank Masashi Kamogawa and an anonymous referee for constructive reviews. We declare we do not have any financial conflict of interests with any organizations.

Data availability statements

For Japanese earthquakes (1994 Hokkaido-toho-oki, 2003 Tokachi-oki, and 2011 Tohoku-oki), we used data from a dense network of GNSS stations, currently known as GEONET (GNSS Earth Observation Network). The data are available from terras.gsi.go.jp after registration. The South American GNSS data for the 2010 Maule earthquake were downloaded from RAMSAC webpage (https://www.ign.gob.ar/NuestrasActividades/Geodesia/Ramsac/DescargaRinex) and from CDDIS (https://cddis.nasa.gov/Data_and_Derived_Products/GNSS/daily_30second_data.html) and UNAVCO (https://www.unavco.org/data/gps-gnss/gps-gnss.html). SUGAR data (www.earthobservatory.sg/facilities/field-installations/sumatran-gps-array-sugar) were used to study the 2010 Mentawai earthquake.

References

Ammon, C. H., H. Kanamori, T. Lay, & A. A. Velasco (2006), The 17 July 2006 Java tsunami earthquake, *Geophys. Res. Lett., 33*, L24308, doi:10.1029/2006GL028005.

Astafyeva, E. (2019), Ionospheric detection of natural hazards, *Rev. Geophysics, 57*, 1265‐1288, doi:10.1029/2019RG000668.

Astafyeva, E. & K. Heki (2009), Dependence of waveform of near-field coseismic ionospheric disturbances on focal mechanisms, *Earth Planets Space, 61*, 939-943, doi:10.1186/BF03353206.

Astafyeva, E., K. Heki, V. Kiryushkin, E. Afraimovich, & S. Shalimov (2009), Two-mode long-distance propagation of coseismic ionosphere disturbances, *J. Geophys. Res., 114*, A10307, doi:10.1029/2008JA013853.

Bagiya, M. Ss, A.S. Sunil, L. Rolland, S. Nayak, M. Ponraj, D. Thomas, D.S. Ramesh (2019), Mapping the impact of non-tectonic forcing mechanisms on GNSS measured coseismic ionospheric perturbations, *Sci. Rep., 9* (1), 1-15.

Cahyadi, M. N. & K. Heki (2013), Ionospheric disturbances of the 2007 Bengkulu and the 2005 Nias earthquakes, Sumatra, observed with a regional GPS network, *J. Geophys. Res., 118*, 1-11, doi:10.1002/jgra.50208.

Cahyadi, M.N. & K. Heki (2015), Coseismic ionospheric disturbance of the large strike-slip earthquakes in North Sumatra in 2012: M_w dependence of the disturbance amplitudes, *Geophys. J. Int., 200*, 116-129, doi:10.1093/gji/ggu343.

Calais, E. & J. B. Minster (1995), GPS detection of ionospheric perturbations following the January 17, 1994, Northridge earthquake. *Geophys. Res. Lett., 22*, 1045–1048. doi:10.1029/95GL00168.

Georges, T. M. & W. H. Hooke (1970), Wave-induced fluctuations in ionospheric electron content – A model indicating some observational biases, *J. Geophys. Res., 75*, 6295-6308, doi:10.1029/JA075i031p06295.

Hargreaves, J. K. (1992), The solar-terrestrial environment. Cambridge University Press, Cambridge, doi:10.1017/CB09780511628924.

He, L. & K. Heki (2016), Three-dimensional distribution of ionospheric anomalies prior to three large earthquakes in Chile, *Geophys. Res. Lett., 43*, 7287-7293, doi:10.1002/2016GL069863.

Heki, K. and J.-S. Ping (2005), Directivity and apparent velocity of the coseismic ionospheric disturbances observed with a dense GPS array, *Earth Planet. Sci. Lett., 236*, 845-855.

Heki, K. and T. Fujimoto (2022), Atmospheric modes excited by the 2021 August eruption of the Fukutoku-Okanoba volcano, Izu-Bonin Arc, observed as harmonic TEC oscillations by QZSS, *Earth Planets Space, 74*, 27, doi:10.1186/s40623-022-01587-5.

Heki, K. (2021), Chapter 21: Ionospheric disturbances related to earthquakes, in *Ionospheric Dynamics and Applications, Geophys. Monograph, 260*, edited by C. Huang, G. Lu, Y. Zhang, and L. J. Paxton, pp.511-526, Wiley/American Geophysical Union, ISBN:978-1-119-50755-0, doi:10.1002/9781119815617.ch21, 2021.

Jin, S., G. Occhipinti, & R. Jin (2015), GNSS ionospheric seismology: Recent observation evidences and characteristics, *Earth Sci. Rev., 147*, 54-64, doi:10.1016/j.earscirev.2015.05.003.

Jin, S., R. Jin, & X. Liu (2018), GNSS Atmospheric Seismology, Springer.

Kanamori, H. (1972), Mechanism of tsunami earthquake, *Phys. Earth Planet. Inter., 6*, 346-359, doi:10.1016/0031-9201(72)90058-1.

Kikuchi, M. & H. Kanamori (1995), The Shikotan Earthquake of October 4, 1994: Lithospheric earthquake, *Geophys. Res. Lett, 22,* 1025-1028, doi:10.1029/95GL00883.

Lay, T., C. J. Ammon, H. Kanamori, Y. Yamazaki, K. F. Cheung, & A. R. Hutko (2011), The 25 October 2010 Mentawai tsunami earthquake (Mw7.8) and the tsunami hazard presented by shallow megathrust ruptures, *Geophys. Res. Lett., 38*, L06302, doi:10.1029/2010GL046552.

Makela, J.J., P. Lognonné, H. Hébert, T. Gehrels, L. Rolland, S. Allgeyer, A. Kherani, G. Occhipinti, E. Astafyeva, P. Coïsson, A. Loevenbruck, E. Clévédé, M.C. Kelley, & J. Lamouroux (2011), Imaging and modelling the ionospheric response to the 11 March 2011 Sendai tsunami over Hawaii, *Geophys. Res. Lett., 38*, L00G02, doi:10.1029/2011GJ047860.

Manta, F., G. Occhipinti, L. Feng, & E. M. Hill (2020), Rapid identification of tsunamigenic earthquakes using GNSS ionospheric sounding, *Sci. Rep., 10*, 11054, doi:10.1038/s41598-020-68097-w.

Matsumura, M., A. Saito, T. Iyemori, H. Shinagawa, T. Tsugawa, Y. Otsuka, M. Nishioka, & Ch. H. Chen (2011), Numerical simulation of atmospheric waves excited by the 2011 off the Pacific coast of Tohoku earthquake, *Earth Planets Space, 63*, 885-889, doi:10.5047/eps.2011.07.015.

Meng, X., P. Vergados, A. Komjathy, & O. Verkhoglyadova (2019), Upper atmospheric responses to surface disturbances: An observational perspective, *Radio Sci., 54*, 1076-1098, doi:10.1029/2019RS006858.

Occhipinti, G., E. A. Kherani, & P. Lognonné (2008), Geomagnetic dependence of ionospheric disturbances induced by tsunamigenic internal gravity waves, *Geophys. J. Int, 173*, 753-765, doi:10.1111/j.1365-246X.2008.03760.x.

Pulido, N., Y. Yagi, H. Kumagai, & N. Nishimura (2011), Rupture process and coseismic deformations of the 27 February 2010 Maule earthquake, Chile, *Earth Planets Space, 63*, 955-959, doi:10.5047/eps.2011.04.008.

Satake, K., Y. Nishimura, P. S. Putra, A. R. Gusman, H. Sunendar, Y. Fujii, Y. Tanioka, H. Latief, & E. Yulianto (2013), Tsunami source of the 2010 Mentawai, Indonesia earthquake inferred from tsunami field survey and waveform modeling, *Pure Applied Geophys., 170*, 1567-1582, doi:10.1007/s00024-012-0536-y.

Savastano, G., A. Komjathy, O. Verkhoglyadova, A. Mazzoni, M. Crespi, Y. Wei, and A. J. Mannucci (2017), Real-time detection of tsunami ionospheric disturbances with a stand-alone GNSS receiver: A preliminary feasibility demonstration, *Sci. Rep., 7*, 46607, doi: 10.1038/srep46607.

Tanimoto, T., C. Ji, & M. Igarashi (2012), An approach to detect afterslips in giant earthquakes in the normal-mode frequency band, *Geophys. J. Int., 190*, 1097-1110, doi:10.1111/j.1365-246X.2012.05524.x.

Tanimoto, T., K. Heki, & J. Artru-Lambin (2015), Interaction of Solid Earth, Atmosphere, and Ionosphere. in *Treatise on Geophysics, 2nd edition, Vol 4*., edited by Gerald Schubert, Oxford: Elsevier, pp. 421-443.

Tanioka, Y. & K. Satake (1996), Fault parameters of the 1896 Sanriku tsunami earthquake estimated from tsunami numerical modeling, *Geophys. Res. Lett., 23*, 1549-1552, doi:10.1029/96GL01479.

Yagi, Y. (2004), Source rupture process of the 2003 Tokachi-oki earthquake determined by joint inversion of teleseismic body wave and strong ground motion data, *Earth Planets Space, 56* (3), 311-316, doi:10.1186/BF03353057.

Yagi, Y., & Y. Fukahata (2011), Rupture process of the 2011 Tohoku-oki earthquake and absolute elastic strain release, *Geophys. Res. Lett., 38*, L19307, doi:10.1029/2011GL048701.

Geophysical Research Letters

Supporting Information for

Slow Fault Slip Signatures in Coseismic Ionospheric Disturbances

K. Heki[1,2], M. S. Bagiya[3], and Y. Takasaka[2]

[1]Shanghai Astronomical Observatory, Chinese Academy of Sciences, Shanghai, China

[2]Dept. Earth Planet. Sci., Hokkaido University, Sapporo, Japan

[3]Indian Institute of Geomagnetism, Mumbai, India

Contents of this file

Introduction

Six figures (Figures S1-S6) are given as the supporting information to help readers better understand the work. They are all quoted in the main text.

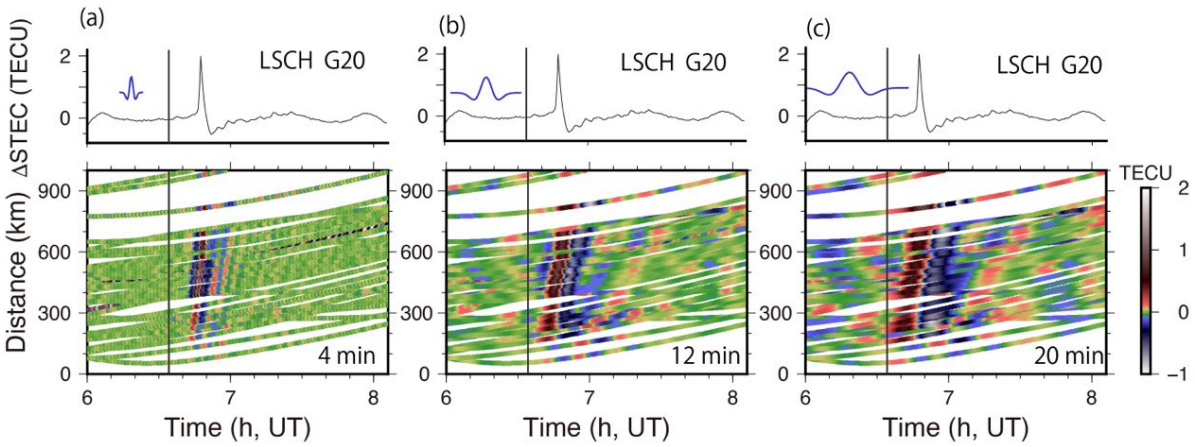

Figure S1. Comparison of the results with wavelet transformation of various periods, 4 minutes (a), 12 minutes (b), and 20 minutes (c), for detecting the coseismic ionospheric disturbance signals of the 2010 Maule earthquake. At the top, a typical time series of slant TEC changes (station: LSCH, satellite: G20, residual from degree 7 best-fit polynomial) is given together with the employed wavelets (blue curves). The 4-minutes wavelet (a) is suitable for highlighting AW components but makes IGW components invisible. IGW emerges as we increase the wavelet period to 12 minutes (b) and 20 minutes (c). Wavelet transformation is performed directly for raw STEC time series (not for the residuals from best-fit polynomials).

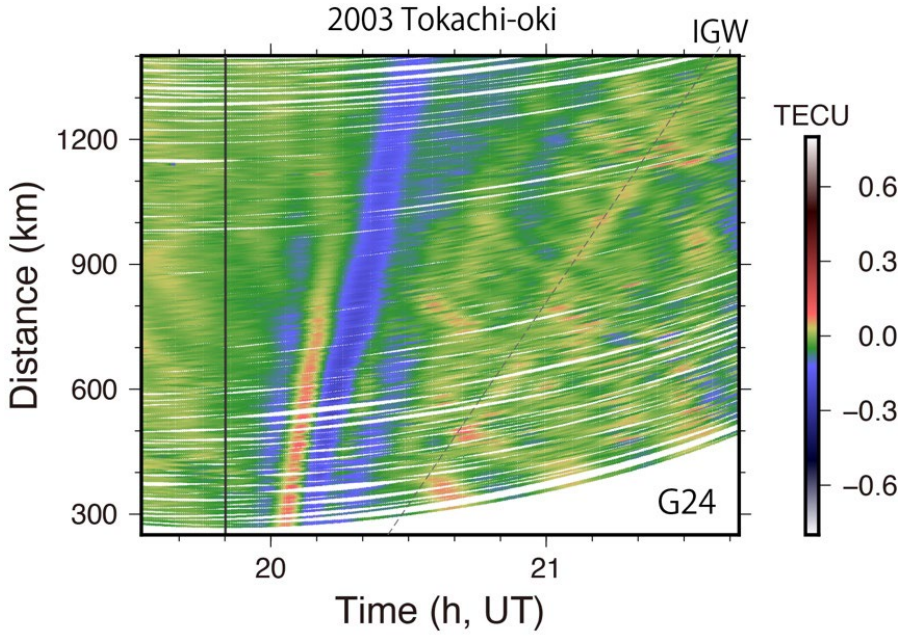

Figure S2. A time-distance plot of coseismic ionospheric disturbances for the 2003 Tokachi-oki earthquake drawn using satellite G24 with a 12-minutes wavelet. After AW, a faint IGW signature is seen. The dashed line along IGW is drawn assuming appearance of 20 minutes after earthquake and propagating at a speed of 0.27 km/s.

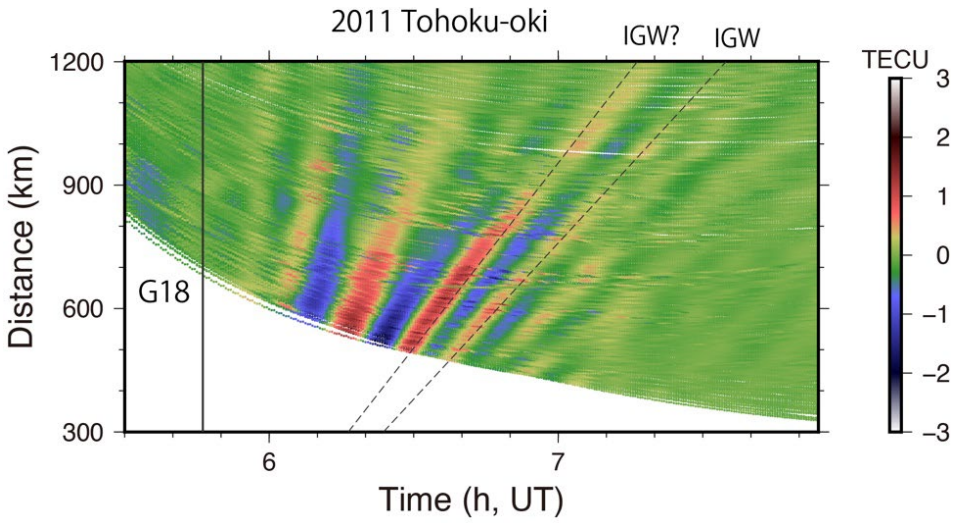

Figure S3. A time-distance plot of coseismic ionospheric disturbances for the 2011 Tohoku-oki earthquake drawn using G18 satellite with a 12-minutes wavelet. There are a few signatures propagating with the IGW speed. We considered the one along the dashed line marked as "IGW" (0.21 km/s starting 14 minutes after earthquake) as the IGW signature propagating from the epicenter (indicated as "A" in Fig.1 of Matsumura et al., 2011). An earlier wave (0.25 km/s starting 10 minutes after earthquake) marked as "IGW?", might be a hybrid wave, i.e., IGW excited by AW that reached the ionosphere ("B" in Fig.1 of Matsumura et al., 2011).

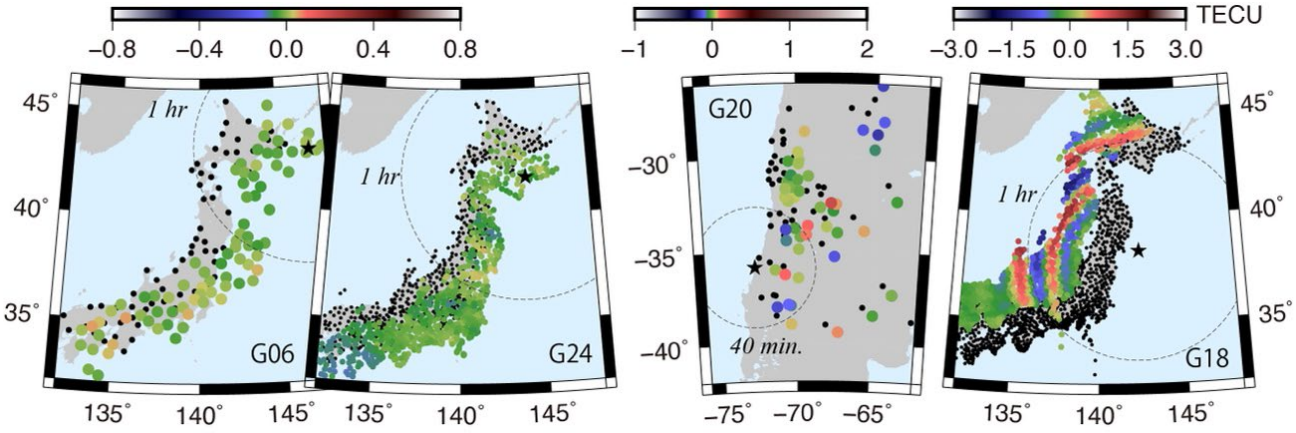

Figure S4. GNSS station positions (black dots) and SIP positions 1 hour (40 min. for Maule) after the 1994 Hokkaido-toho-oki, 2003 Tokachi-oki, 2010 Maule, and 2011 Tohoku-oki earthquakes, from left to right. Colors of SIP show the wavelet transformation values given in Figure 1, and S2-3.

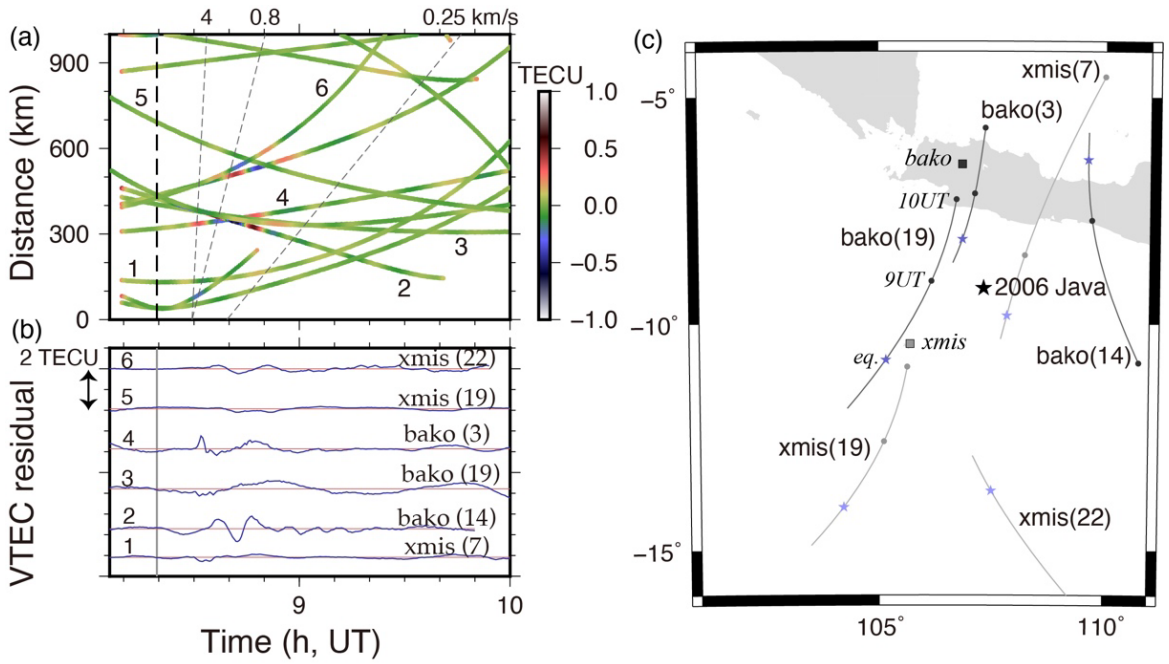

Figure S5. (a) A time-distance plot drawn using two IGS stations, xmis and bako, close to the 2006 Java earthquake epicenter. IGW signatures are supposed to lie along the slope of 0.25 km/s, but they are not clear in this figure. VTEC time series (residuals from degree 4 polynomials) of six selected station-satellite pairs are given in (b). AW origin disturbances are clear, e.g., in the bako-G3 pair, it is difficult to identify the IGW signatures. (c) SIP trajectory for the six station-satellite pairs during the period shown in (b). Circles and stars on the trajectory indicate the hourly time marks and the earthquake occurrence time, respectively.

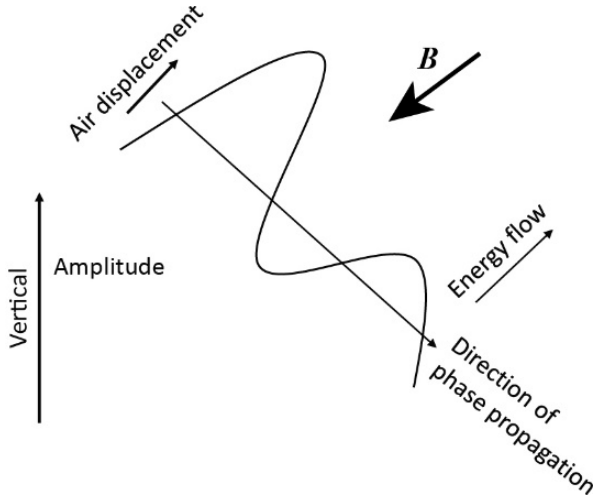

Figure S6. Geometry of particle motion in IGW after Hargreaves (1992). In the ionospheric F region, interaction of moving electrons and geomagnetic fields (B) controls the growth of electron density anomalies to some extent.